



## Article

# Crystal Structure Evolution of Piezoelectric Fe-Doped ZnO Film by Magnetron Co-Sputtering Technique

Ya-Chih Cheng<sup>1</sup>, Sanjaya Brahma<sup>1</sup>, Sean Wu<sup>2</sup> , Jow-Lay Huang<sup>1</sup> and Alex C. H. Lee<sup>3,4,\*</sup>

<sup>1</sup> Department of Materials Science and Engineering, National Cheng Kung University, Tainan 70101, Taiwan; jlh888@mail.ncku.edu.tw (J.-L.H.)

<sup>2</sup> Department of Semiconductor Engineering, Lunghwa University of Science and Technology, Taoyuan 333326, Taiwan; wusean.tw@gmail.com

<sup>3</sup> Department of Mechanical Engineering, National Chin-Yi University of Technology, Taichung 411030, Taiwan

<sup>4</sup> Department of Green Energy, National University of Tainan, Tainan 70005, Taiwan

\* Correspondence: alexchlee@ncut.edu.tw; Tel.: +886-933-531-372

**Abstract:** Zinc oxide (ZnO) exhibits piezoelectric properties due to its asymmetric structure, making it suitable for piezoelectric devices. This experiment deposited Fe-doped ZnO films on silicon substrates using a dual-target magnetron co-sputtering system. The films achieved a high c-axis orientation, and the piezoelectric coefficient of the film reached its optimal value of 44.35 pC/N when doped with 0.5 at% of Fe. This value is approximately three times that of undoped ZnO films with a piezoelectric coefficient of 13.04 pC/N. The study utilized a diffractometer, scanning electron microscopy, transmission electron microscopy, and atomic force microscopy to evaluate the crystal structure evolution of the zinc oxide films and employed X-ray photoelectron spectroscopy to assess the valence state of the Fe ions.

**Keywords:** ZnO; Fe dopant; piezoelectric film; crystal structure



Academic Editor: Yoshikazu Mizuguchi

Received: 27 November 2024

Revised: 2 January 2025

Accepted: 10 January 2025

Published: 15 January 2025

**Citation:** Cheng, Y.-C.; Brahma, S.; Wu, S.; Huang, J.-L.; Lee, A.C.H. Crystal Structure Evolution of Piezoelectric Fe-Doped ZnO Film by Magnetron Co-Sputtering Technique. *Condens. Matter* **2025**, *10*, 6. <https://doi.org/10.3390/condmat10010006>

**Copyright:** © 2025 by the authors. Licensee MDPI, Basel, Switzerland. This article is an open access article distributed under the terms and conditions of the Creative Commons Attribution (CC BY) license (<https://creativecommons.org/licenses/by/4.0/>).

## 1. Introduction

ZnO nanomaterials, which crystallize in either cubic zinc blende or hexagonal wurtzite structures or exist in various forms such as nanowires, nanofilms, nanopowders, etc. [1,2], have been widely investigated for a variety of functional applications. These electronic or energy-related functional applications primarily stem from the ease of manufacturing ceramic nanomaterials and controlling their physical properties by adjusting crystal structures. A deeper look reveals that the root of the crystal structure or phase stability of these ZnO nanomaterials lies in the type of chemical bonds. The difference in electronegativity between the oxygen anion and zinc cation is equal to  $3.44 - 1.65 = 1.79$ , determining the nature of Zn-O bonding is ionic [3] (i.e., the electronegativity range of 1.6 to 2.0 is considered to exhibit a high degree of ionic character and a smaller portion of polar covalent character). Furthermore, if the size of a solute cation is similar to that of a Zn ion, the solute cation would enter into a ZnO crystal, thus forming a substitutional solid solution. As ZnO is a host material, its morphology and properties can be controlled by inserting impurities/dopants or by various synthesis routes. Among these synthesizing strategies, the magnetron sputtering technique enables the preparation of well-crystallized ZnO thin films with the desired thickness at a scale of several  $\mu\text{m}$  [4]. ZnO films are suitable for various technological domains, such as transparent conducting films or electrodes in solar energy cells [5,6], acoustic wave devices [7], pressure sensors [8], photodetectors [9], etc.

Piezoelectricity is the conversion between mechanical energy and electricity. Piezoelectric materials are dielectric materials that rely on molecular polarization to exhibit

piezoelectric properties. In thin film materials, each crystal generates surface charges, and the amount of polarization results from summing the contributions from each wurtzite crystal with the polarization component along the c-axis. The concept of doping wurtzite piezoelectric structures started with Sc-doped AlN in 2009 [10]. Subsequently, Cr [11] or Yb [12] dopants can effectively improve the piezoelectric performance of aluminum nitride films, thus directly enhancing the sensitivity and efficiency of the devices. Several research groups have also attempted to analyze results using computer simulations to identify potential alternatives to the costly Sc dopant [13,14]. The development of ScAlN piezoelectric film is highly suitable for applications in surface acoustic wave devices for fifth-generation mobile communication technology [15]. Although AlN films are suitable for high-temperature operating environments and exhibit excellent stability, making them ideal for high-frequency filters, their high manufacturing cost limits their application. When considering manufacturing costs, ZnO films are more suitable than AlN films for low-end biosensors or low-frequency filter applications. ZnO exhibits superior piezoelectric properties, making it highly effective for fabricating high-sensitivity liquid sensors [16]. However, ZnO films are prone to forming defects, negatively affecting their piezoelectric performance and stability. Therefore, improving film deposition techniques to minimize defects is a critical research topic, as this would further accelerate the application of ZnO piezoelectric films in 5G technology.

The piezoelectric coefficient describes the materials' response to the piezoelectric effect, represented by  $d_{33}$  (C/N) [17]. The typical  $d_{33}$  value for undoped ZnO with a wurtzite structure is 8 pC/N determined by experiments [18] or 12.84 pC/N determined by simulation [19]. The  $d_{33}$  values of ZnO films with various dopants have been reported. ZnO films containing Mn [20], Mg [21], Cr [22], Y [23], Eu [24], and V [25] dopants have  $d_{33}$  values of 86, 59.1, 120, 49.6, 43.38, and 85 pC/N, respectively. The piezoelectric coefficient of ZnO nanomaterials is enhanced due to piezoelectric polarization and lattice distortion of the ZnO lattice by differences in ionic radii of various dopants that might lead to variations in electronegativity and chemical bonding strength [26]. In addition to these dopants, iron is earth-abundant and cost-efficient and can achieve the piezoelectric enhancement of ZnO thin films with a doping amount of less than 2% [27]. In this work, we will discuss the phase stability and structural evolution of Fe-doped ZnO films and investigate the critical structural factors contributing to the enhancement of the piezoelectric coefficient.

## 2. Results

### 2.1. Article Content

#### 2.1.1. Deposition Behavior of the Fe-Doped ZnO Films

The compositions of each Fe/ZnO film were measured by energy dispersive spectrometer (EDS) in atomic % (at%). As the RF power of the  $\text{Fe}_2\text{O}_3$  target increases during sputtering, the Fe concentration of the films gradually increases while the Zn concentration slightly decreases. It was noted that the total concentration of Fe and Zn remained almost constant. In this co-sputtering system, since argon is used as the working gas, the resulting ZnO film is expected to be an n-type semiconductor. The formation of oxygen vacancies is accompanied by the generation of two free electrons, thereby enhancing the conductivity of this piezoelectric material. The XRD patterns of pure ZnO and Fe-doped ZnO films deposited onto Si (100) substrates were shown in Figure 1a. These oxide films exhibited a wurtzite structure with a strong preferred orientation along the [0002] direction. According to the literature [28,29], a single Bragg diffraction peak was observed, indicating a ZnO crystal structure with a high c-axis orientation. The ZnO with a zinc blende structure does not exhibit any characteristic peaks within this diffraction angle range. In ZnO thin film materials, a shift in the diffraction peak position is typically associated with film strain

induced by heterojunctions [30] or doping effects in the ZnO material [31]. Furthermore, according to the Scherrer equation, broadening of the diffraction peak is related to the refinement of ZnO crystallite size [32]. In this study, the ZnO thin films grown along the [0002] plane exhibited an a-axis lattice constant of 0.325 nm, while the a-axis lattice constant of the Si substrate with a (100) plane was 0.543 nm. Thus, when the two materials were joined, the interface experienced tensile stress, leading to an increase in the lattice constant. Consequently, the [0002] diffraction peak angle slightly shifts to a higher value compared to the theoretical value (i.e., the theoretical angle of the [0002] diffraction peak is  $34.228^\circ$  based on the JCPDS no. 36-1451) as shown in Figure 1b. When a small amount of Fe ions was doped, including the three samples with “<0.1 at% Fe (5W)”, “<0.1 at% Fe (10W)”, and “0.5 at% Fe”, the Bragg angle of the [0002] diffraction peak slightly increased, while the diffraction peak shape remained unchanged. This phenomenon indicated that a small amount of Fe ion doping reduced the lattice constant of ZnO. However, when a higher amount of Fe ions was doped, including the two samples with “1.8 at% Fe” and “4.7 at% Fe”, the Bragg angle of the [0002] diffraction peak began to decrease, and the diffraction peak broadened. This suggested that higher levels of Fe ion doping increase the lattice constant of ZnO and indicate the possibility of crystallite refinement. The current shift in the XRD diffraction peaks may be related to the doping of Fe ions, which will be further discussed in terms of changes in the oxidation state of Fe ions. The broadening of the XRD diffraction peaks may be associated with the grain morphology, and this will be corroborated with subsequent FESEM analysis results. However, we will still assess the relationship among cation radii, lattice volume, and Bragg angle. Based on the effective ionic radii table for the selected six-coordinated ions proposed by Shannon [33], the ionic radii of  $\text{Fe}^{3+}$ ,  $\text{Fe}^{2+}$ , and  $\text{Zn}^{2+}$  are 78 pm, 92 pm, and 88 pm, respectively. Consequently, when  $\text{Fe}^{3+}$  substitutes  $\text{Zn}^{2+}$  in ZnO materials, the lattice volume contracted, leading to a rightward shift in the diffraction angle. Conversely, when  $\text{Fe}^{2+}$  substituted  $\text{Zn}^{2+}$  in ZnO materials, the lattice volume underwent a slight expansion, resulting in a leftward shift in the diffraction angle.

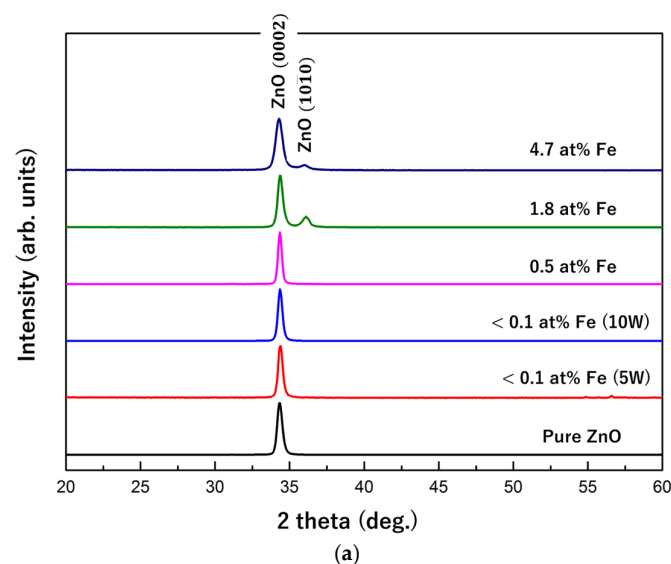
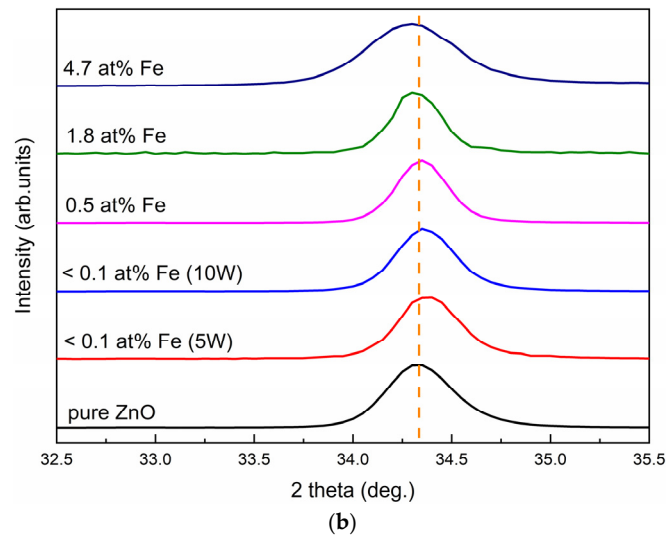


Figure 1. Cont.

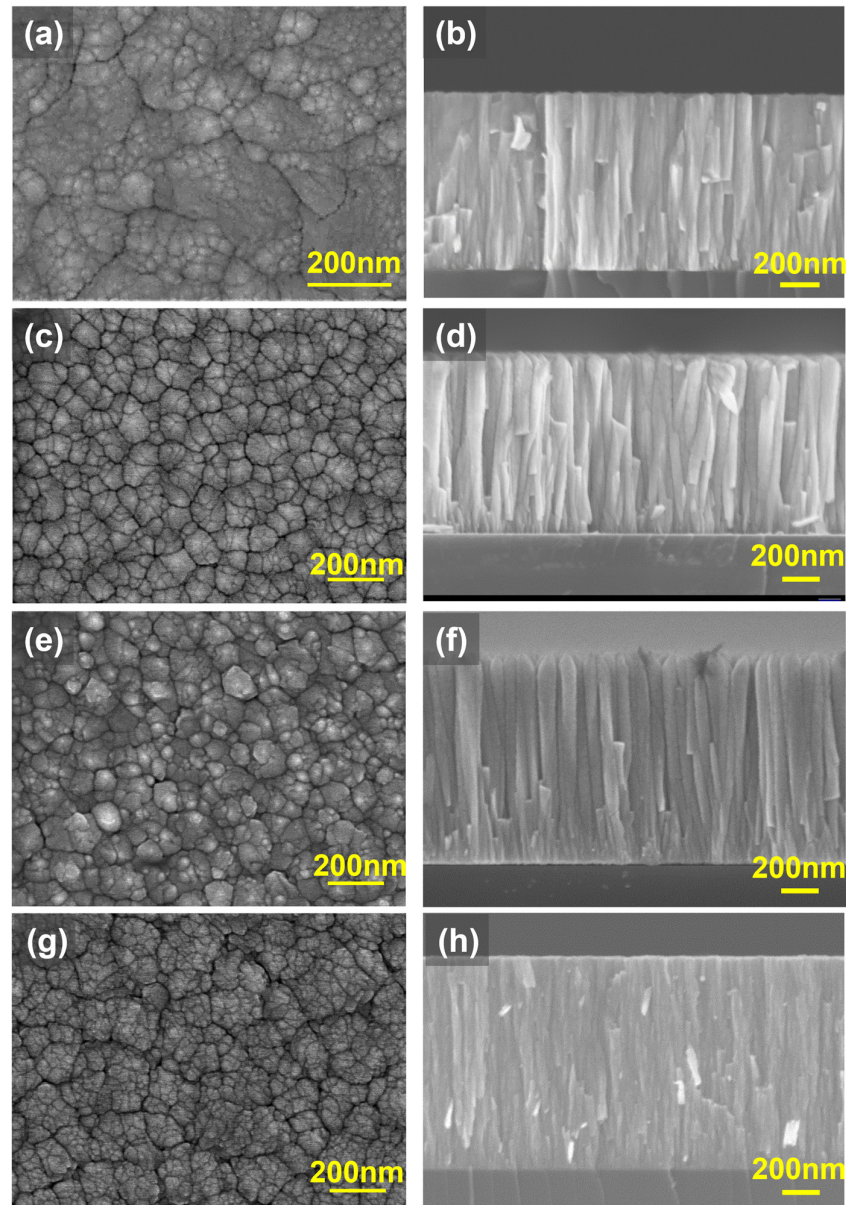


**Figure 1.** The XRD diffraction curves of pure ZnO and Fe/ZnO films deposited by RF magnetron sputtering, ranging (a)  $20^{\circ}$ – $60^{\circ}$  and (b)  $32.5^{\circ}$ – $35.5^{\circ}$  with a slow scanning rate.

### 2.1.2. Crystal Structure of the Fe-Doped ZnO Films

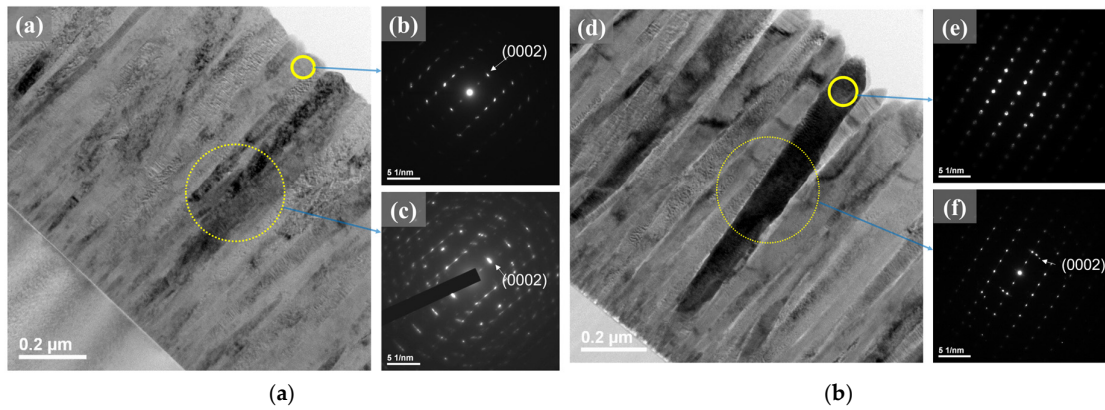
Figure 2 demonstrated the FESEM plan view and cross-sectional images of Fe-doped ZnO thin films (i.e., pure ZnO for (a,b), ZnO film with Fe concentration of 0.5 at% for (c,d), 1.8 at% for (e,f), and 4.7 at% for (g,h)). The surface morphology of pure ZnO was characterized by large aggregates of rounded particles (Figure 2a). However, after doping with 0.5 at% of Fe, these large aggregates disappeared, and the size distribution of the rounded particles became more uniform (Figure 2c). With the increase in the Fe concentration, the grain size became smaller as shown in Figure 2e,g. This is because the doped Fe atoms raised the activation energy for grain growth, thereby inhibiting grain coarsening [34]. The grain refinement observed in the FESEM analysis is consistent with the broadening of the [0002] diffraction peak observed in the XRD analysis. The cross-sectional images in Figure 2b,d,f,h suggested that all films grew with a columnar nanorod-like microstructures with thicknesses around  $1\ \mu\text{m}$ , implying RF magnetron sputtering is suitable for the preparation of films with preferred orientation. The cross-sectional images also demonstrated a sharp interface between the Si substrate and the Fe/ZnO films. In addition, the ZnO films exhibit a smooth surface compared to a rougher texture in the doped ZnO films with Fe concentrations of 0.5 and 1.8 at%. As Fe concentration was 4.7 at%, the observed roughness of the Fe/ZnO film was similar to that of pure ZnO film.

Figure 3 demonstrates the bright-field TEM cross-sectional microstructure of the (a) pure ZnO and (d) Fe/ZnO (1.8 at% Fe) films. As observed from the two images, both of the deposited films had a thickness of about  $1\ \mu\text{m}$  and exhibited straight and parallel nanorod morphology that grew perpendicular to the Si substrate. Figure 3b,e show the typical selective area diffraction (SAD) patterns with zone axis  $[10\bar{1}0]$  recorded at the tip of one nanorod-like grain in pure ZnO and Fe/ZnO films, respectively (as marked by a solid-line circle), verifying that each nanorod is single-crystalline. Figure 3c,f represent  $[10\bar{1}0]$  SAD patterns recorded from a large area (as marked by dash-line circles) that were covered with several nanorods. These areas have a similar crystallographic orientation to the single nanorod. At the same time, the splitting diffraction spots can be observed. The results strongly suggest that pure ZnO and Fe/ZnO films are polycrystals.

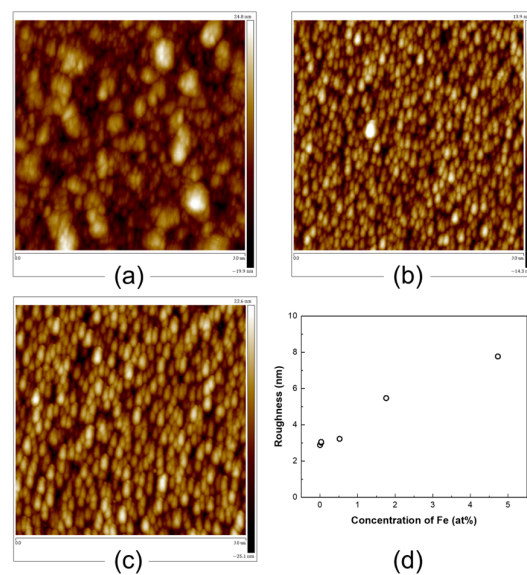


**Figure 2.** FESEM images of the sputtered films. (a,b) Pure ZnO film and Fe/ZnO films with (c,d) 0.5 at%, (e,f) 1.8 at%, (g,h) 4.7 at%. Among these figures, (a,c,e,g) are plane-view images, and (b,d,f,h) are cross-sectional images.

Figure 4 shows the representative surface morphologies and roughness as probed by AFM. The pure ZnO film exhibited large island-like grains (Figure 4a). As Fe content reached 0.5 at%, the surface grains became needle-like (Figure 4b). As Fe concentration is 1.8 at%, nanorod-like morphology became more distinct, probably due to the formation of bigger grains in the Fe-doped ZnO phase (Figure 4c). However, if too much Fe was incorporated, the needle-like structure reverted to a large island-like structure. Figure 4d is the surface roughness of the films with different Fe concentrations. When the Fe content increased, the film's roughness gradually increased. The increase in roughness may be due to the higher power used for the  $\text{Fe}_2\text{O}_3$  target. Higher power gives the sputtered atoms higher energy, allowing them a greater chance of diffusing and moving upon adsorption to the substrate, resulting in an overall increase in roughness [35]. It is apparent that the results of this AFM experiment are consistent with the conclusions drawn from the SEM.



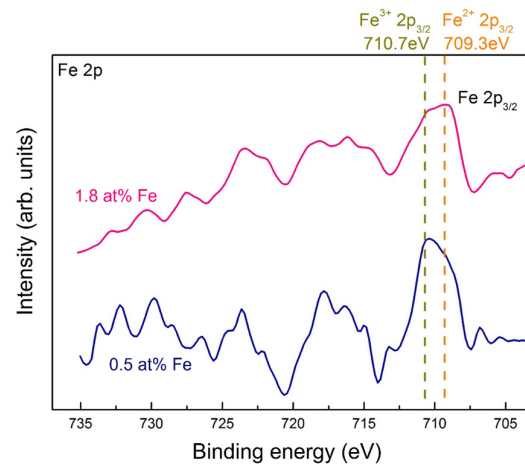
**Figure 3.** Cross-sectional TEM bright-field images of (a) ZnO and (d) Fe/ZnO film with Fe content of 1.8 at%. (b,c) are the selected area diffraction patterns of the circled area as shown in (a). (e,f) are the selected area diffraction patterns of the circled area, as shown in (d).



**Figure 4.** AFM images of sputtered films. (a) Pure ZnO film, and Fe/ZnO film with (b) 0.5 at%, (c) 1.8 at% Fe concentration. (d) The surface roughness of the deposited film with various Fe concentrations.

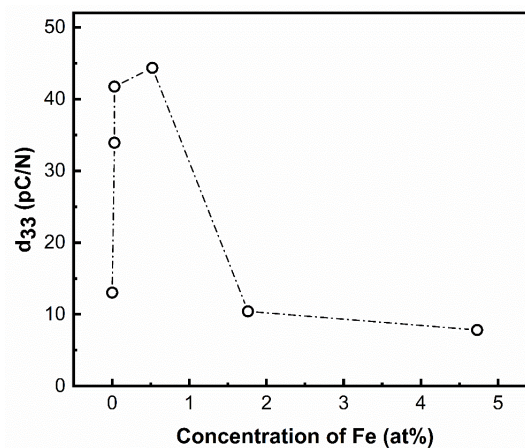
### 2.1.3. Piezoelectric Properties of the Fe-Doped ZnO Films

Figure 5 displays the binding energy analysis of the Fe 2p orbital using XPS in the energy section of 700–740 eV for the Fe-doped ZnO films with Fe concentrations of 0.5 at% and 1.8 at% and considering the thin film with 0.5 at% Fe content peaked at 710.50 eV, close to the  $\text{Fe}^{3+} 2p_{3/2}$  peak value of 710.7 eV in  $\text{Fe}_2\text{O}_3$ , as reported in the literature [36]. On the other hand, the thin film had 1.8 at% Fe content had a peak at 708.9 eV, close to the  $\text{Fe}^{2+} 2p_{3/2}$  peak value of 709.3 eV in FeO. Therefore, it could be inferred that the Fe ion in the doped ZnO film containing 0.5 at% Fe has a +3 oxidation state, while the Fe ion in the doped ZnO film containing 1.8 at% Fe has a +2 oxidation state. Liu et al. [37] utilized XPS analysis to investigate the changes in binding energy states of Fe-doped ZnO nanoparticles. The analysis revealed that the Fe ions predominantly existed in the form of  $\text{Fe}^{3+}$ , with a small amount of  $\text{Fe}^0$ , while the zinc ions were primarily in the chemical state of  $\text{Zn}^{2+}$ . The results indicated that the doping of Fe ions altered the surface chemical environment of the ZnO material and affected its electronic structure. The results of this study are highly consistent with the analysis conducted by Liu et al. [37].



**Figure 5.** The binding energy analysis by XPS for representative Fe/ZnO films.

Figure 6 shows the variation in the piezoelectric coefficient with Fe concentration. It can be seen that the piezoelectric coefficient of the pure ZnO thin film deposited using our experimental equipment is 13.04 pC/N (compared to 12.4 pC/N for undoped pure zinc oxide thin films reported in the literature [19]). As the power of the Fe<sub>2</sub>O<sub>3</sub> target increases, the Fe content in the film increases, resulting in an initial rise followed by a sharp decrease in the piezoelectric coefficient of the Fe-doped ZnO thin film. The maximum piezoelectric response occurred when the Fe content was 0.5 at% in the doped ZnO film. The highest piezoelectric coefficient is 44.35 pC/N. When the Fe content reaches 1.8 at%, the piezoelectric coefficient drops sharply to a low value of 10.43 pC/N. As the Fe concentration increases to 4.7 at%, the piezoelectric coefficient decreases to 7.83 pC/N.



**Figure 6.** Piezoelectric coefficient of sputtered films as a function of Fe concentration.

### 3. Discussion

The change in piezoelectric coefficients is closely related to the variation in the material's nanostructure. The following are some causes that may degrade piezoelectric properties: (1) As shown in XRD patterns in Figure 1, it is observed that for the sample with Fe concentration of 1.8 at%, the relative intensity of the peak in the [0002] plane of ZnO began to decrease. This appearance of the (10 $\bar{1}$ 1) plane might decrease the degree of preferred orientation along the c-axis, thus reducing the effective dipole moment, thereby leading to a decrease in the material's piezoelectric coefficient; (2) considering grain characteristics as demonstrated by SEM, TEM, and AFM, the samples with the optimal piezoelectric coefficient exhibit a more uniform grain distribution, while excessive Fe ion doping leads to excessive grain refinement and generates an increased number of grain boundaries. The

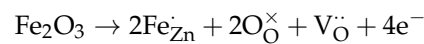
high density of grain boundaries might impede electron transfer, thereby reducing the piezoelectric coefficient; (3) as observed from XPS results (Figure 6), it can be confirmed that a significant enhancement of the piezoelectric coefficient is due to the smaller radii of Fe ions with a +3 oxidation state, facilitating lattice distortion originating from bond rotation. In contrast, the larger radii of Fe ions with a +2 oxidation state make bond rotation more complex, decreasing piezoelectric performance.

ZnO thin films are generally prone to oxygen vacancies, which result in the formation of n-type semiconductors [38]. By appropriately doping with trivalent ions such as Fe or Al [39], the electron concentration in ZnO films can be enhanced. On the other hand, doping with monovalent ions such as Li [40] allows for tuning the carrier type in ZnO films. With regard to relevant defect chemistry, the doping elements under sputtering conditions can lead to the formation of different kinds of defects. The following uses Fe<sub>2</sub>O<sub>3</sub>-doped ZnO materials in this work as an example:

(I) Under conditions of higher oxygen partial pressure:



(II) Under conditions of lower oxygen partial pressure:



Condition I occurs when the oxygen partial pressure is relatively high, forming Zn vacancies in ZnO films. Condition II occurs when the oxygen partial pressure is relatively low, forming oxygen vacancies and free electrons in ZnO films. The co-sputtering system used in this study belongs to condition II. When the Fe ion concentration was less than 2 at%, the valence state was 3+, resulting in a significant increase in the concentration of free electrons, thereby enhancing the piezoelectric properties. It can be noted that these defects can introduce additional free electrons, which enhance the sensitivity and efficiency of piezoelectric thin films or alter the bandgap width of ZnO materials. Due to the influence of these defects, ZnO has been widely utilized in piezoelectric semiconductors, sensing elements, and optical materials. Kumar and Kim [41] reported that ZnO can be used in piezoelectric energy harvesters to convert mechanical energy from the environment into electrical energy. Bui et al. [42] noted that controlling the grain size and crystal orientation of ZnO thin films can improve their piezoelectric performance. Shiang et al. [21] demonstrated that Mg-doped ZnO thin films could modulate the bandgap width, making them suitable for ultraviolet photodetectors. Al- or Ga-doped ZnO thin films, used as window layers in solar cells, enhance ultraviolet absorption properties and improve photovoltaic conversion efficiency [43,44]. Additionally, Song et al. [45] revealed that Al-doped ZnO films could adjust the refractive index and bandgap width, enabling the fabrication of high-performance anti-reflective coatings for optical lens surfaces. In LED applications, Pearton and Ren [46] indicated that heterostructures formed between n-type ZnO films and p-type materials could effectively increase the recombination efficiency of free electrons and defects, enhancing light emission performance. When used as photocatalytic materials, Zayed et al. [47] and Cwik et al. [48] also noted that doped ZnO thin films improve visible light absorption, thereby increasing the efficiency of photocatalytic water splitting or degradation of organic pollutants. In summary, doped ZnO thin films enhance the reliability of semiconductor sensing devices and strengthen the applications of various optical materials, contributing to the sustainable development of the global environment.

#### 4. Materials and Methods

The Fe/ZnO thin films were grown on p-type Si substrate with an orientation of (100) using the radio frequency magnetron co-sputtering technique with ZnO (99.99% purity,

two inches in diameter) and Fe<sub>2</sub>O<sub>3</sub> (99.99% purity, two inches in diameter) as targets. The substrates were cleaned sequentially with acetone, isopropanol, and D.I. water for 10 min. The working pressure was evacuated to  $4.0 \times 10^{-2}$  torr using a diffusion pump. The deposition gases of Ar (purity > 99.9995%) were introduced into the chamber at a flow rate of 30 sccm. The substrate rotation speed was controlled at 15 rpm. The distances between the substrate and targets (ZnO and Fe<sub>2</sub>O<sub>3</sub>) were about 5 cm, respectively. The targets were pre-sputtered for 5–10 min to remove surface contamination. A constant power of 100 W was maintained at the ZnO target, while the applied powers of Fe<sub>2</sub>O<sub>3</sub> were tuned to adjust Fe concentration in Fe/ZnO films. All the depositions were conducted at room temperature, and the film thickness was controlled at about 1  $\mu$ m.

X-ray diffractometer (XRD, Multiflex DD3517, Rigaku, Tokyo, Japan) and field-emission scanning electron microscopy (FESEM, Zeiss Auriga, Carl Zeiss AG., Jena, Germany) were used to examine the crystal phase and microstructure of Fe-doped ZnO thin films. The atomic percent (at%) of individual elements, including Fe, Zn, O, etc., in the thin films was determined by an EDS equipped with FESEM. An atomic force microscope (AFM) was also used to observe the surface morphology of the films and determine their roughness. X-ray photoelectron spectroscopy (XPS) was employed to confirm the binding energy of Fe and Zn. The piezoelectric coefficient was measured by a piezoresponse force microscope, which includes a commercial scanning probe microscope (SPM, Bruker multi-mode, Bruker, Billerica, MA, USA.) equipped with a Veeco Nanoscope V controller (Veeco Instruments Inc., Plainview, NY, USA).

## 5. Conclusions

The highly c-axis-oriented, wurtzite-structured Fe/ZnO films were deposited on Si substrates using the magnetron co-sputtering technique. The XRD results showed that as Fe content is smaller than 1 at%, only the [0002] plane is present. When Fe concentration in the doped ZnO films is 1~5 at%, the (10 $\bar{1}$ 1) plane gradually appears. The SEM and TEM images also confirmed that pure ZnO and Fe-doped ZnO films mainly comprise nanorod-like single crystals grown along the [0002] direction. The thin film with the best piezoelectric performance comes from the doped ZnO film with an Fe concentration of 0.5 at%. Its piezoelectric coefficient (44.35 pC/N) is four times higher than that of pure ZnO film. The XPS results indicate that the Fe<sup>3+</sup> substitution mechanism is the leading cause of enhancing the piezoelectric performance of doped ZnO film with Fe concentration less than 1 at%. The degradation mechanisms for piezoelectric performance of doped ZnO film containing 1.8 and 4.7 at% of Fe concentration come from the appearance of the (10 $\bar{1}$ 1) plane (deduced from XRD results), grain refinement (deduced from SEM and AFM results), and Fe<sup>2+</sup> substitution (deduced from XPS data).

**Author Contributions:** Conceptualization, S.W., J.-L.H. and A.C.H.L.; data curation, A.C.H.L.; formal analysis, Y.-C.C., S.B., S.W., J.-L.H. and A.C.H.L.; funding acquisition, A.C.H.L.; investigation, Y.-C.C. and S.W.; methodology, Y.-C.C. and J.-L.H.; project administration, A.C.H.L.; supervision, S.W., J.-L.H. and A.C.H.L.; validation, A.C.H.L.; visualization, Y.-C.C.; writing—original draft, A.C.H.L.; Writing—review and editing, S.B., J.-L.H. and A.C.H.L. All authors have read and agreed to the published version of the manuscript.

**Funding:** This research was funded by the National Science and Technology Council (NSTC), Taiwan, with the project number: NSTC 113-2221-E-167-009-.

**Data Availability Statement:** The data supporting the findings of this study are available from the corresponding author upon reasonable request.

**Conflicts of Interest:** The authors declare no conflicts of interest.

## References

1. Sharma, D.K.; Shukla, S.; Sharma, K.K.; Kumar, V. A review on ZnO: Fundamental properties and applications. *Mater. Today Proc.* **2022**, *49*, 3028–3035. [[CrossRef](#)]
2. Rai, R.S.; Bajpai, V.; Khan, M.I.; Elboughdiri, N.; Shanableh, A.; Luque, R. An eco-friendly approach on green synthesis, bio-engineering applications, and future outlook of ZnO nanomaterial: A critical review. *Environ. Res.* **2023**, *221*, 114807. [[CrossRef](#)] [[PubMed](#)]
3. Steven, S.; Zumdahl, D.J.D. *AE Chemical Principles*, 8th ed.; Cengage: Boston, MA, USA, 2017.
4. Abdallah, B.; Zetoun, W.; Tello, A. Deposition of ZnO thin films with different powers using RF magnetron sputtering method: Structural, electrical and optical study. *Heliyon* **2024**, *10*, e27606. [[CrossRef](#)] [[PubMed](#)]
5. Badgujar, A.C.; Yadav, B.S.; Jha, G.K.; Dhage, S.R. Room Temperature Sputtered Aluminum-Doped ZnO Thin Film Transparent Electrode for Application in Solar Cells and for Low-Band-Gap Optoelectronic Devices. *ACS Omega* **2022**, *7*, 14203–14210. [[CrossRef](#)]
6. Sarma, B.K.; Rajkumar, P. Al-doped ZnO transparent conducting oxide with appealing electro-optical properties—Realization of indium free transparent conductors from sputtering targets with varying dopant concentrations. *Mater. Today Commun.* **2020**, *23*, 100870. [[CrossRef](#)]
7. Zhao, X.; Zhao, M.; Peng, W.; He, Y. Review of bulk acoustic wave resonant optical detectors. *Sens. Actuators A Phys.* **2023**, *355*, 114333. [[CrossRef](#)]
8. Yin, J.; Guo, S.; E, M.; Liu, H.; Liu, Z.; Ding, W.; Li, D.; Cui, Y. Self-Powered Rapid Response Flexible Pressure Sensor for Wearable Application. *Adv. Eng. Mater.* **2023**, *25*, 2201678. [[CrossRef](#)]
9. Wang, J.; Chen, C.; Jin, M.; Zhu, Y.; Zhang, N. The carbon dots modified ZnO films photodetector with broadband and fast photoresponse. *Opt. Mater.* **2023**, *135*, 113341. [[CrossRef](#)]
10. Akiyama, M.; Kano, K.; Teshigahara, A. Influence of growth temperature and scandium concentration on piezoelectric response of scandium aluminum nitride alloy thin films. *Appl. Phys. Lett.* **2009**, *95*, 162107. [[CrossRef](#)]
11. Luo, J.T.; Fan, B.; Zeng, F.; Pan, F. Influence of Cr-doping on microstructure and piezoelectric response of AlN films. *J. Phys. D Appl. Phys.* **2009**, *42*, 235406. [[CrossRef](#)]
12. Hirata, K.; Mori, Y.; Yamada, H.; Uehara, M.; Anggraini, S.A.; Akiyama, M. Significant Enhancement of Piezoelectric Response in AlN by Yb Addition. *Materials* **2021**, *14*, 309. [[CrossRef](#)] [[PubMed](#)]
13. Iwazaki, Y.; Yokoyama, T.; Nishihara, T.; Ueda, M. Highly enhanced piezoelectric property of co-doped AlN. *Appl. Phys. Express* **2015**, *8*, 061501. [[CrossRef](#)]
14. Startt, J.; Quazi, M.; Sharma, P.; Vazquez, I.; Poudyal, A.; Jackson, N.; Dingreville, R. Unlocking AlN Piezoelectric Performance with Earth-Abundant Dopants. *Adv. Electron. Mater.* **2023**, *9*, 2201187. [[CrossRef](#)]
15. Chung, C.-Y.; Chen, Y.-C.; Chen, Y.-C.; Kao, K.-S.; Chang, Y.-C. Fabrication of a 3.5-GHz Solidly Mounted Resonator by Using an AlScN Piezoelectric Thin Film. *Coatings* **2021**, *11*, 1151. [[CrossRef](#)]
16. Huang, H.-Y.; Chiang, H.-J.; Wu, C.-Z.; Lin, Y.; Shen, Y.-K. Analysis on Characteristics of ZnO Surface Acoustic Wave with and without Micro-Structures. *Micromachines* **2019**, *10*, 434. [[CrossRef](#)]
17. Eitel, R.E. *Novel Piezoelectric Ceramics: Development of High Temperature, High Performance Piezoelectrics on the Basis of Structure*; The Pennsylvania State University: University Park, PA, USA, 2003.
18. Hutson, A.R. Piezoelectricity and Conductivity in ZnO and CdS. *Phys. Rev. Lett.* **1960**, *4*, 505–507. [[CrossRef](#)]
19. Karanth, D.; Fu, H. Large electromechanical response in ZnO and its microscopic origin. *Phys. Rev. B* **2005**, *72*, 064116. [[CrossRef](#)]
20. Luo, J.T.; Zhu, X.Y.; Chen, G.; Zeng, F.; Pan, F. Influence of the Mn concentration on the electromechanical response  $d_{33}$  of Mn-doped ZnO films. *Phys. Status Solidi (RRL)—Rapid Res. Lett.* **2010**, *4*, 209–211. [[CrossRef](#)]
21. Shiao, J.-S.; Brahma, S.; Huang, J.-L.; Liu, C.-P. Fabrication of flexible UV-B photodetectors made of  $Mg_xZn_{1-x}O$  films on PI substrate for enhanced sensitivity by piezophototronic effect. *Appl. Mater. Today* **2020**, *20*, 100705. [[CrossRef](#)]
22. Yang, Y.C.; Song, C.; Wang, X.H.; Zeng, F.; Pan, F. Cr-substitution-induced ferroelectric and improved piezoelectric properties of  $Zn_{1-x}Cr_xO$  films. *J. Appl. Phys.* **2008**, *103*, 074107. [[CrossRef](#)]
23. Cheng, L.-C.; Brahma, S.; Huang, J.-L.; Liu, C.-P. Enhanced piezoelectric coefficient and the piezoelectric nanogenerator output performance in Y-doped ZnO thin films. *Mater. Sci. Semicond. Process* **2022**, *146*, 106703. [[CrossRef](#)]
24. Yadav, H.; Sinha, N.; Goel, S.; Kumar, B. Eu-doped ZnO nanoparticles for dielectric, ferroelectric and piezoelectric applications. *J. Alloy. Compd.* **2016**, *689*, 333–341. [[CrossRef](#)]
25. Laurenti, M.; Castellino, M.; Perrone, D.; Asvarov, A.; Canavese, G.; Chiolerio, A. Lead-free piezoelectrics: V<sup>3+</sup> to V<sup>5+</sup> ion conversion promoting the performances of V-doped Zinc Oxide. *Sci. Rep.* **2017**, *7*, 41957. [[CrossRef](#)] [[PubMed](#)]
26. Kingery, W.D.; Chiang, Y.M.; Birnie, D.P. *David Kingery. Physical Ceramics: Principles for Ceramic Science and Engineering*; Wiley: New York, NY, USA, 1996.
27. Luo, J.T.; Yang, Y.C.; Zhu, X.Y.; Chen, G.; Zeng, F.; Pan, F. Enhanced electromechanical response of Fe-doped ZnO films by modulating the chemical state and ionic size of the Fe dopant. *Phys. Rev. B* **2010**, *82*, 014116. [[CrossRef](#)]

28. García-Gancedo, L.; Pedrós, J.; Zhu, Z.; Flewitt, A.J.; Milne, W.I.; Luo, J.K.; Ford, C.J.B. Room-temperature remote-plasma sputtering of c-axis oriented zinc oxide thin films. *J. Appl. Phys.* **2012**, *112*, 014907. [[CrossRef](#)]
29. Manzano, C.V.; Alegre, D.; Caballero-Calero, O.; Alén, B.; Martín-González, M.S. Synthesis and luminescence properties of electrodeposited ZnO films. *J. Appl. Phys.* **2011**, *110*, 043538. [[CrossRef](#)]
30. Chebil, W.; Fouzri, A.; Fargi, A.; Azeza, B.; Zaaboub, Z.; Sallet, V. Characterization of ZnO thin films grown on different p-Si substrate elaborated by solgel spin-coating method. *Mater. Res. Bull.* **2015**, *70*, 719–727. [[CrossRef](#)]
31. Srinivasulu, T.; Saritha, K.; Reddy, K.T.R. Synthesis and characterization of Fe-doped ZnO thin films deposited by chemical spray pyrolysis. *Mod. Electron. Mater.* **2017**, *3*, 76–85. [[CrossRef](#)]
32. Otis, G.; Ejgenberg, M.; Mastai, Y. Solvent-Free Mechanochemical Synthesis of ZnO Nanoparticles by High-Energy Ball Milling of  $\epsilon$ -Zn(OH)<sub>2</sub> Crystals. *Nanomaterials* **2021**, *11*, 238. [[CrossRef](#)]
33. Shannon, R.D. Revised effective ionic radii and systematic studies of interatomic distances in halides and chalcogenides. *Acta Crystallogr. Sect. A* **1976**, *32*, 751–767. [[CrossRef](#)]
34. Tanahashi, M.; Ito, M.; Murao, M.; Iga, A. Effect of Al-doping on the Grain Growth of ZnO. *Jpn. J. Appl. Phys.* **1997**, *36*, L573. [[CrossRef](#)]
35. Le, M.-T.; Sohn, Y.U.; Lim, J.; Choi, G.S. Effect of Sputtering Power on the Nucleation and Growth of Cu Films Deposited by Magnetron Sputtering. *Mater. Trans.* **2010**, *51*, 116–120. [[CrossRef](#)]
36. Mills, P.; Sullivan, J.L. A study of the core level electrons in iron and its three oxides by means of X-ray photoelectron spectroscopy. *J. Phys. D Appl. Phys.* **1983**, *16*, 723. [[CrossRef](#)]
37. Liu, C.; Meng, D.; Pang, H.; Wu, X.; Xie, J.; Yu, X.; Chen, L.; Liu, X. Influence of Fe-doping on the structural, optical and magnetic properties of ZnO nanoparticles. *J. Magn. Magn. Mater.* **2012**, *324*, 3356–3360. [[CrossRef](#)]
38. Özgür, Ü.; Alivov, Y.I.; Liu, C.; Teke, A.; Reshchikov, M.A.; Doğan, S.; Avrutin, V.; Cho, S.-J.; Morkoç, H. A comprehensive review of ZnO materials and devices. *J. Appl. Phys.* **2005**, *98*, 041301. [[CrossRef](#)]
39. Taabouche, A.; Bouabellou, A.; Kermiche, F.; Hanini, F.; Sedrati, C.; Bouachiba, Y.; Benazzouz, C. Preparation and characterization of Al-doped ZnO piezoelectric thin films grown by pulsed laser deposition. *Ceram. Int.* **2016**, *42*, 6701–6706. [[CrossRef](#)]
40. Chang, Y.-T.; Chen, J.-Y.; Yang, T.-P.; Huang, C.-W.; Chiu, C.-H.; Yeh, P.-H.; Wu, W.-W. Excellent piezoelectric and electrical properties of lithium-doped ZnO nanowires for nanogenerator applications. *Nano Energy* **2014**, *8*, 291–296. [[CrossRef](#)]
41. Kumar, B.; Kim, S.-W. Energy harvesting based on semiconducting piezoelectric ZnO nanostructures. *Nano Energy* **2012**, *1*, 342–355. [[CrossRef](#)]
42. Bui, Q.C.; Salem, B.; Roussel, H.; Mescot, X.; Guerfi, Y.; Jiménez, C.; Consonni, V.; Ardila, G. Effects of thermal annealing on the structural and electrical properties of ZnO thin films for boosting their piezoelectric response. *J. Alloys Compd.* **2021**, *870*, 159512. [[CrossRef](#)]
43. Jun, M.-C.; Park, S.-U.; Koh, J.-H. Comparative studies of Al-doped ZnO and Ga-doped ZnO transparent conducting oxide thin films. *Nanoscale Res. Lett.* **2012**, *7*, 639. [[CrossRef](#)]
44. Amala Rani, A.; Ernest, S. Structural, morphological, optical and compositional characterization of spray deposited Ga doped ZnO thin film for Dye-Sensitized Solar Cell application. *Superlattices Microstruct.* **2014**, *75*, 398–408. [[CrossRef](#)]
45. Song, J.; Sun, J.; Lian, Y.; Tao, W.; Xie, Y.; Yang, Y. High-performance antireflection nanostructure arrays on aluminum-doped zinc oxide film fabricated with femtosecond laser near-field processing. *Appl. Surf. Sci.* **2023**, *615*, 156353. [[CrossRef](#)]
46. Pearton, S.J.; Ren, F. Advances in ZnO-based materials for light emitting diodes. *Curr. Opin. Chem. Eng.* **2014**, *3*, 51–55. [[CrossRef](#)]
47. Zayed, M.; Ahmed, A.M.; Shaban, M. Synthesis and characterization of nanoporous ZnO and Pt/ZnO thin films for dye degradation and water splitting applications. *Int. J. Hydrogen Energy* **2019**, *44*, 17630–17648. [[CrossRef](#)]
48. Ćwik, K.; Zawadzki, J.; Zybala, R.; Ożga, M.; Witkowski, B.; Wojnar, P.; Wolska-Pietkiewicz, M.; Jędrzejewska, M.; Lewiński, J.; Borysiewicz, M.A. Magnetron Sputtering as a Solvent-Free Method for Fabrication of Nanoporous ZnO Thin Films for Highly Efficient Photocatalytic Organic Pollution Degradation. *Compounds* **2024**, *4*, 534–547. [[CrossRef](#)]

**Disclaimer/Publisher’s Note:** The statements, opinions and data contained in all publications are solely those of the individual author(s) and contributor(s) and not of MDPI and/or the editor(s). MDPI and/or the editor(s) disclaim responsibility for any injury to people or property resulting from any ideas, methods, instructions or products referred to in the content.